



# Superexchange-induced Pt-O-Ti<sup>3+</sup> site on single photocatalyst for efficient H<sub>2</sub> production with organics degradation in wastewater

Tao Zhang<sup>a</sup>, Zhiyong Zhao<sup>a</sup>, Dongpeng Zhang<sup>a</sup>, Xingyu Liu<sup>b</sup>, Pengfei Wang<sup>c,1</sup>, Yi Li<sup>d</sup>, and Sihui Zhan<sup>a,1</sup>

Edited by Alexis Bell, University of California, Berkeley, CA; received February 19, 2023; accepted April 24, 2023

Efficient photocatalytic H<sub>2</sub> production from wastewater instead of pure water is a dual solution to the environmental and energy crisis, but due to the rapid recombination of photoinduced charge in the photocatalyst and inevitable electron depletion caused by organic pollutants, a significant challenge of dual-functional photocatalysis (simultaneous oxidative and reductive reactions) in single catalyst is designing spatial separation path for photogenerated charges at atomic level. Here, we designed a Pt-doped BaTiO<sub>3</sub> single catalyst with oxygen vacancies (BTPO<sub>v</sub>) that features Pt-O-Ti<sup>3+</sup> short charge separation site, which enables excellent H<sub>2</sub> production performance (1519 μmol·g<sup>-1</sup>·h<sup>-1</sup>) while oxidizing moxifloxacin ( $k = 0.048 \text{ min}^{-1}$ ), almost 43 and 98 times than that of pristine BaTiO<sub>3</sub> (35 μmol·g<sup>-1</sup>·h<sup>-1</sup> and  $k = 0.00049 \text{ min}^{-1}$ ). The efficient charge separation path is demonstrated that the oxygen vacancies extract photoinduced charge from photocatalyst to catalytic surface, and the adjacent Ti<sup>3+</sup> defects allow rapid migration of electrons to Pt atoms through the superexchange effect for H<sup>+</sup> adsorption and reduction, while the holes will be confined in Ti<sup>3+</sup> defects for oxidation of moxifloxacin. Impressively, the BTPO<sub>v</sub> shows an exceptional atomic economy and potential for practical applications, a best H<sub>2</sub> production TOF (370.4 h<sup>-1</sup>) among the recent reported dual-functional photocatalysts and exhibiting excellent H<sub>2</sub> production activity in multiple types of wastewaters.

wastewater hydrogen evolution | asymmetric Pt-O-Ti<sup>3+</sup> sites | superexchange | dual-functional photocatalysis | carbon neutrality

Persistent organic contaminants enriched in wastewater pose a considerable risk to the health of both humans and ecosystems (1, 2). Advanced oxidation processes (Fenton process, photochemistry, electrochemistry and so on) achieve water purification through directly destroying antibiotics by strong oxidizing radicals, and their treatment processes are often accompanied by a substantial amount of energy input and waste of organic compounds in water (3, 4). An appealing treatment option for this problem is the dual-functional photocatalytic process, which allows the simultaneous recovery of clean energy (H<sub>2</sub>) during water treatment. The basic principle of the process is to utilize both the oxidation energy of holes and the reduction energy of electrons in one system, which requires achieving efficient separation of electrons and holes at different sites (5). The current research mainly focuses on the construction of multicomponent heterojunctions, which can vectorially transfer generated electron-hole pairs into different photocatalysts (6, 7). However, lattice mismatch often leads to loss of charge transfer at the interfaces of heterostructures, while multicomposites usually signify complex synthesis methods and higher costs, which are not favorable for practical applications (8, 9). The construction of dual reaction sites in single catalysts to enable simultaneous oxidative and reductive reactions is an effective way to address these issues (10). However, there are still two fundamental challenges to overcome.

The first challenge regarding dual-functional photocatalysis is the photoinduced charge transfer from the photocatalyst bulk to surface (11). In general, the “energy pumping and delivering” process of photoinduced charge separation and subsequent transfer is considered a critical step in photocatalytic efficiency, and the high recombination rate of electrons and holes inside the catalyst still restricts the utilization of photogenerated electrons and holes (12, 13). As shown in Fig. 1A, the light irradiation causes the catalyst to move from the ground state to excited state, and the valence band electrons gain enough energy to leap into the empty conduction band (14, 15). The strong ionic character of metal oxides makes the lattice susceptible to self-trapping with photoinduced charges to form polaron states (electron-phonon coupling), which then return to the ground state by hot-carrier cooling or nonradiative recombination (16, 17). Surface defects can act as trapping sites to extract photogenerated charges from the bulk of photocatalyst, but the trapped electrons

## Significance

Efficient photocatalytic H<sub>2</sub> production from wastewater and simultaneous degradation of multiple types of pollutants (without the addition of sacrificial agents or peroxides) is an effective way to achieve carbon neutrality. However, the charge recombination occurs on a much faster timescale (ps-ms) than photocatalytic surface reactions (ms-s), which seriously limits the dual-functional photocatalytic activity. Herein, asymmetric Pt-O-Ti<sup>3+</sup> site brings dynamic charge separation efficiency at the picosecond level through the superexchange effect, while achieving site synergy for simultaneous redox reactions in a single catalyst. This provided insights for develop advanced catalysts by coupling various challenging reactions through physically relevant effects in a single catalyst.

Author contributions: T.Z., P.W., and S.Z. designed research; T.Z., Z.Z., D.Z., X.L., Y.L., and S.Z. analyzed data; and T.Z., P.W., Y.L., and S.Z. wrote the paper.

The authors declare no competing interest.

This article is a PNAS Direct Submission.

Copyright © 2023 the Author(s). Published by PNAS. This article is distributed under Creative Commons Attribution-NonCommercial-NoDerivatives License 4.0 (CC BY-NC-ND).

<sup>1</sup>To whom correspondence may be addressed. Email: pengfeiwang@hebut.edu.cn or sihuizhan@nankai.edu.cn.

This article contains supporting information online at <https://www.pnas.org/lookup/suppl/doi:10.1073/pnas.2302873120/-/DCSupplemental>.

Published May 30, 2023.

and holes recombination occurs on a very fast timescale and are difficult to separate and utilize (18).

The second challenge is the targeted migration of surface carriers to the reaction sites, which is crucial to simultaneous oxidative and reductive reactions in single catalyst. Previous research results showed that the recombination time of photogenerated electrons and holes is usually from a few picoseconds to a few microseconds ( $10^{-12}$  to  $10^{-6}$  s), while the timescales of surface oxidation and reduction reactions are microseconds to seconds ( $10^{-6}$  to 10 s) (19, 20). Therefore, due to the random distribution of multiple active sites, unexpectedly long migration paths on catalyst surface can lead to additional electron-hole complexation and reaction resistance. Construction of synergistic active sites with short charge migration paths in a single catalyst enables the

targeted accumulation of electrons and holes, which facilitates the simultaneous oxidation and reduction reactions in one system (10, 12). Perovskite oxides with  $ABO_3$  structure have been reported for various applications, where A and B refer to cations from the rare-earth/alkaline-earth group and transition metal group, respectively (21, 22). Benefiting from the multiple atoms and variable structures, physical correlation effects (Jahn–Teller effect, super-exchange effect and so on) are rich in perovskite oxides, providing a distinctive modulation method for the separation and directed transport of photoinduced charges (23). Moreover, profiting from the ordered B-site ion arrangement, well-defined adjacent catalytic sites facilitate the design of short charge migration pathways, which can catalyze seemingly incompatible oxidation and reduction reactions simultaneously in one system (24). Therefore, it is

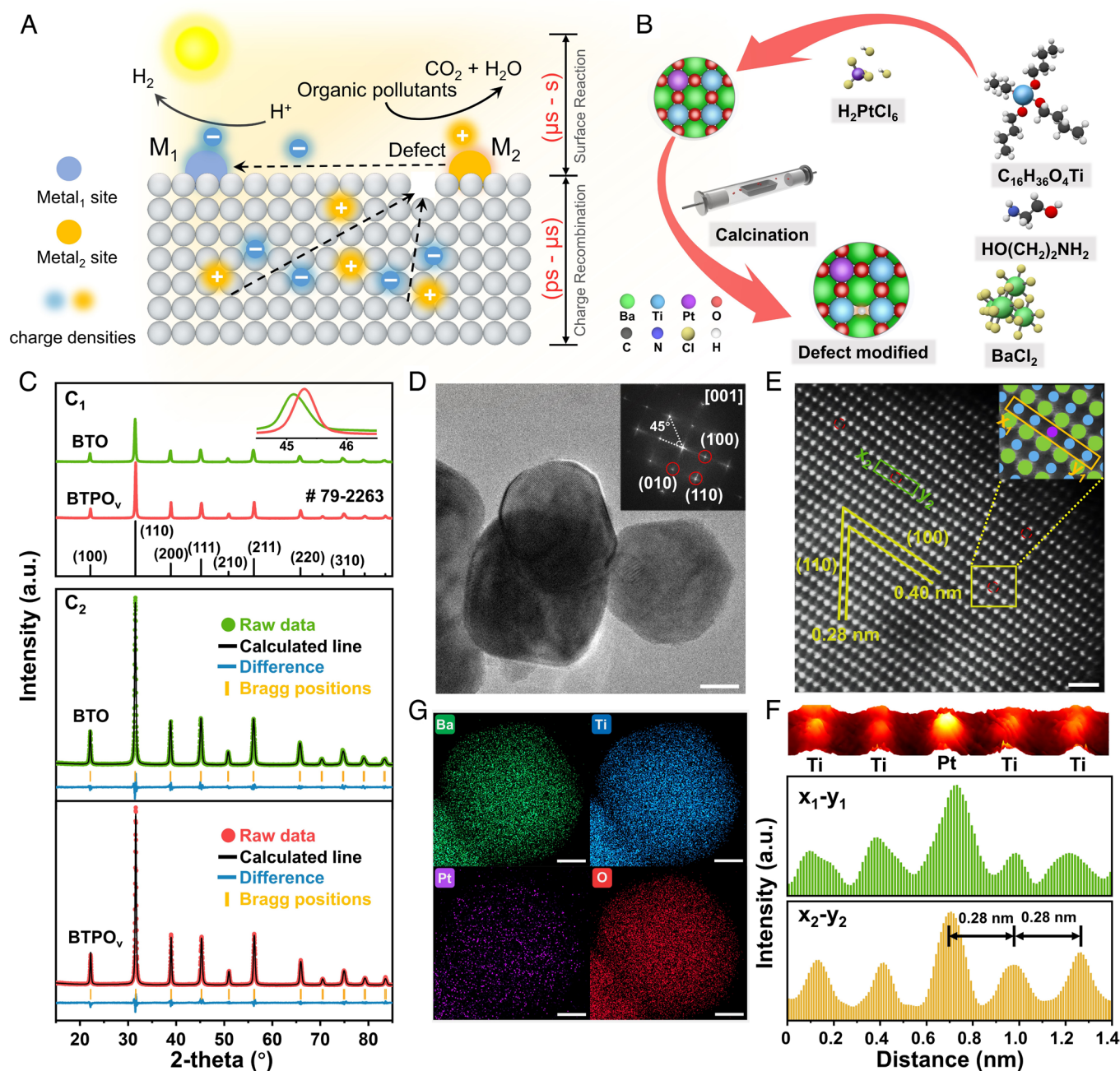


**Fig. 1.** Synthesis and structural characterizations. (A) Schematic illustration of the photoinduced charge transfer process. (B) Synthesis procedure of BTPO<sub>v</sub>. (C) Powder XRD and Refined XRD of BTO and BTPO<sub>v</sub>. (D) TEM image and FFT pattern of BTPO<sub>v</sub>. (E) HAADF-STEM image of BTPO<sub>v</sub>. (F) Surface and line scan measured along the x-y rectangle regions. (G) EDS mapping images of BTPO<sub>v</sub> (Scale bar in D and G is 20 nm and in E is 1 nm.).

feasible to design an ideal perovskite system with short charge migration paths that can separate photogenerated electrons and holes at the atomic-level to avoid recombination of photogenerated carriers.

Herein, we designed a Pt-doped BaTiO<sub>3</sub> single catalyst with oxygen vacancies achieved simultaneous H<sub>2</sub> production for photocatalytic degradation of moxifloxacin (MOX) solution. The catalyst exhibits excellent H<sub>2</sub> production activity (1519 μmol·g<sup>-1</sup>·h<sup>-1</sup>) and degradation kinetic model (*k* value is 0.048 min<sup>-1</sup>) in trace MOX solution (20 mg·L<sup>-1</sup>), which is 43 times and 98 times higher than that of the pristine BaTiO<sub>3</sub>, respectively. Moreover, among the recently reported dual-functional photocatalysts, the optimized catalyst showed better atomic economy with a TOF of 370 h<sup>-1</sup> for hydrogen production. Combining experimental and first-principle density functional theory calculations, the surface oxygen vacancies play the role of extracting photogenerated electrons and holes from photocatalyst to catalytic surface, and the adjacent Ti<sup>3+</sup> defects (3d<sup>1</sup> conformation) allow rapid migration of electrons to Pt atoms through the 180° superexchange effect, while the holes will be confined in Ti<sup>3+</sup> defects for oxidation of MOX. This work brings new insights into the synergy of multiactive site in single catalyst and provides a promising approach to modulation of charge migration through physically relevant effects.

## Results and Discussion

**Surface Structural Characterization.** The synthetic procedure of Pt-doped BaTiO<sub>3</sub> with oxygen vacancies single catalyst is illustrated in Fig. 1*B*. Briefly, the pristine BaTiO<sub>3</sub> was synthesized by a hydrothermal reaction (denoted as BTO). The Pt species were absorbed and anchored on the surface of BTO under water bath conditions, and surface oxygen vacancy was generated by calcining in Ar atmosphere. Among all the samples, the Pt doping of 0.08 wt% showed the best activity and therefore it was selected as the model catalyst (denoted as BTPO<sub>v</sub>). BTO<sub>v</sub> without Pt doping and BTPO without oxygen vacancy were prepared as references (*SI Appendix, Figs. S1–S3*).

The X-ray diffraction (XRD) was initially used to verify the phase structure (Fig. 1*C*<sub>1</sub> and *SI Appendix, Fig. S4*), the symmetric peak at 45° and all Bragg diffraction peaks can well prove the cubic phase of BaTiO<sub>3</sub> (*Pm-3m*, JCPDS No.79-2263) (25). The main peaks of BTPO<sub>v</sub> and BTO<sub>v</sub> are slightly shifted to a higher angle compared to the BTO and BTPO, and Rietveld refinement of XRD (Fig. 1*C*<sub>2</sub> and *SI Appendix, Fig. S5* and *Table S1*) shows the cell parameters of BTPO<sub>v</sub> become smaller than BTO (from 4.018 to 4.012), which was mainly due to the increase of global cubic symmetry (26). In addition, Fourier transform infrared spectra (*SI Appendix, Fig. S6*) and Raman spectra (*SI Appendix, Fig. S7*) also confirm this. The electron paramagnetic resonance spectrum was used to further identify surface defect in the samples (*SI Appendix, Fig. S8*). And the strong asymmetric signals at *g* = 2.003 and *g* = 1.975 correspond to oxygen vacancies and Ti<sup>3+</sup> defects, respectively, which confirm the introduction of oxygen vacancies and Ti<sup>3+</sup> ions in BTPO<sub>v</sub> (27). The transmission electron microscopy (TEM), scanning electron microscopy and Brunauer–Emmett–Teller analysis reveal surface morphology of BTPO<sub>v</sub> (Fig. 1*D* and *SI Appendix, Figs. S9* and *S10* and *Table S2*), all samples show irregular cubic features with a size of about 60 nm, and no obvious differences in particle size and specific surface area are found between BTPO<sub>v</sub> and other samples, which suggests that the surface morphology is not the main reason affecting the photocatalytic activity. Further determination of atomic-level structural information of BTPO<sub>v</sub> was used by high angle annular dark-field scanning transmission electron

microscopy (HAADF-STEM). In Fig. 1*E*, the crystal plane distances of 0.28 nm and 0.40 nm correspond to the (110) and (100) crystal planes of BTPO<sub>v</sub>, indicating that the BTPO<sub>v</sub> has a highly exposed (001) crystal plane; meanwhile, the fast Fourier transform (FFT) image also confirm the high exposure of the [001] crystal plane (Fig. 1*D, Inset*) (28). Note that the atomic number is positively correlated with the brightness of atoms in HAADF-STEM, with Pt (78) atoms being brighter than Ti (22) atoms. Therefore, the local atomic structure of Pt in BTPO<sub>v</sub> can be determined. As shown in Fig. 1*E*, the dispersed bright spots prove the atomic dispersion of the Pt atoms on the BTO surface (29). As further confirm by the selected area (*x-y* rectangle regions in Fig. 1*E*) surface and line intensity plots (Fig. 1*F*), the atomically dispersed Pt atoms enter the lattice by substituting Ti atoms. Furthermore, the EDX element mapping also shows homogeneous distribution of Pt atoms in BTPO<sub>v</sub> catalyst (Fig. 1*G* and *SI Appendix, Fig. S11*).

**Chemical Structure and Coordination Information.** The valence state and precise structural information were further studied by X-ray absorption spectra. The white line intensities of Pt *L*<sub>3</sub>-edge X-ray absorption near edge structure (XANES) of BTPO and BTPO<sub>v</sub> are between those of PtO<sub>2</sub> and Pt foil, indicating that the valence state of Pt atoms is between 0 and +4. And the fitted average valence state are +3.95 and +3.56, respectively. It is demonstrated that the homovalent element Pt prefers substituted Ti atoms to maintain the overall charge neutrality of the catalyst (Fig. 2*A*). The lower Pt valence state in BTPO<sub>v</sub> is due to the creation of oxygen vacancies that redistribute the extra electrons to the adjacent cation site (30). Then, the coordination environments of Pt atoms were confirmed by extended X-ray absorption fine structure (EXAFS). The prominent FT peak of BTPO<sub>v</sub> at 1.59 Å is attributed to the Pt–O bonds, and the bond lengths are shorter than the 1.65 Å of BTPO (Fig. 2*B*), which may be caused by the lattice shrinkage due to oxygen vacancies (31). The Pt *L*-edge wavelet transform (WT)-EXAFS (Fig. 2*C*) shows the same coordination information in both *k* and *R* space, with the maximum at around 4.2 Å<sup>-1</sup> showing the Pt–O coordination feature, and no maximum at 8.3 Å<sup>-1</sup> detected with Pt–Pt coordination, further confirming the atomically dispersed of Pt atoms. Moreover, the coordination information extracted from the fitted curves (Fig. 2*D* and *SI Appendix, Fig. S12*) shows that the BTPO<sub>v</sub> exhibits a shorter bonding environment (1.977 Å) than BTPO (1.994 Å) and the Pt atoms have similar coordination structure in BTPO and BTPO<sub>v</sub> (approximating Pt–O<sub>6</sub>), indicate that no oxygen vacancies directly linked to Pt atom (*SI Appendix, Table S3*) (32, 33). To further identify the relative positions of Pt atoms and oxygen vacancies, first-principle density functional theory (DFT) calculations were performed. The results show that Ti atoms adjacent to Pt atoms produce surface oxygen vacancies with much lower formation energy (0.767 eV), single Pt atoms promote the neighboring TiO<sub>6</sub> units to generate surface oxygen vacancies and form Pt–O–Ti<sup>3+</sup> sites (Fig. 2*E*), which is consistent with the previously reported results (34). All these results qualitatively verify the distinct local atomic arrangement of BTPO<sub>v</sub> (*SI Appendix, Fig. S13*).

**Dual-Functional Photocatalytic Performance.** The photocatalytic performance of MOX degradation integrated with H<sub>2</sub> production was investigated in a MOX solution instead of traditional sacrificial solvents. To optimize the MOX removal rate, the effects of key reaction parameters including the dosages of catalysts and pollutant concentration on the photocatalytic hydrogen evolution (PHE) rate and degradation rate were studied (*SI Appendix, Figs. S14–S17*). The time courses PHE is shown in Fig. 3*A* and *SI Appendix, Fig. S18*.

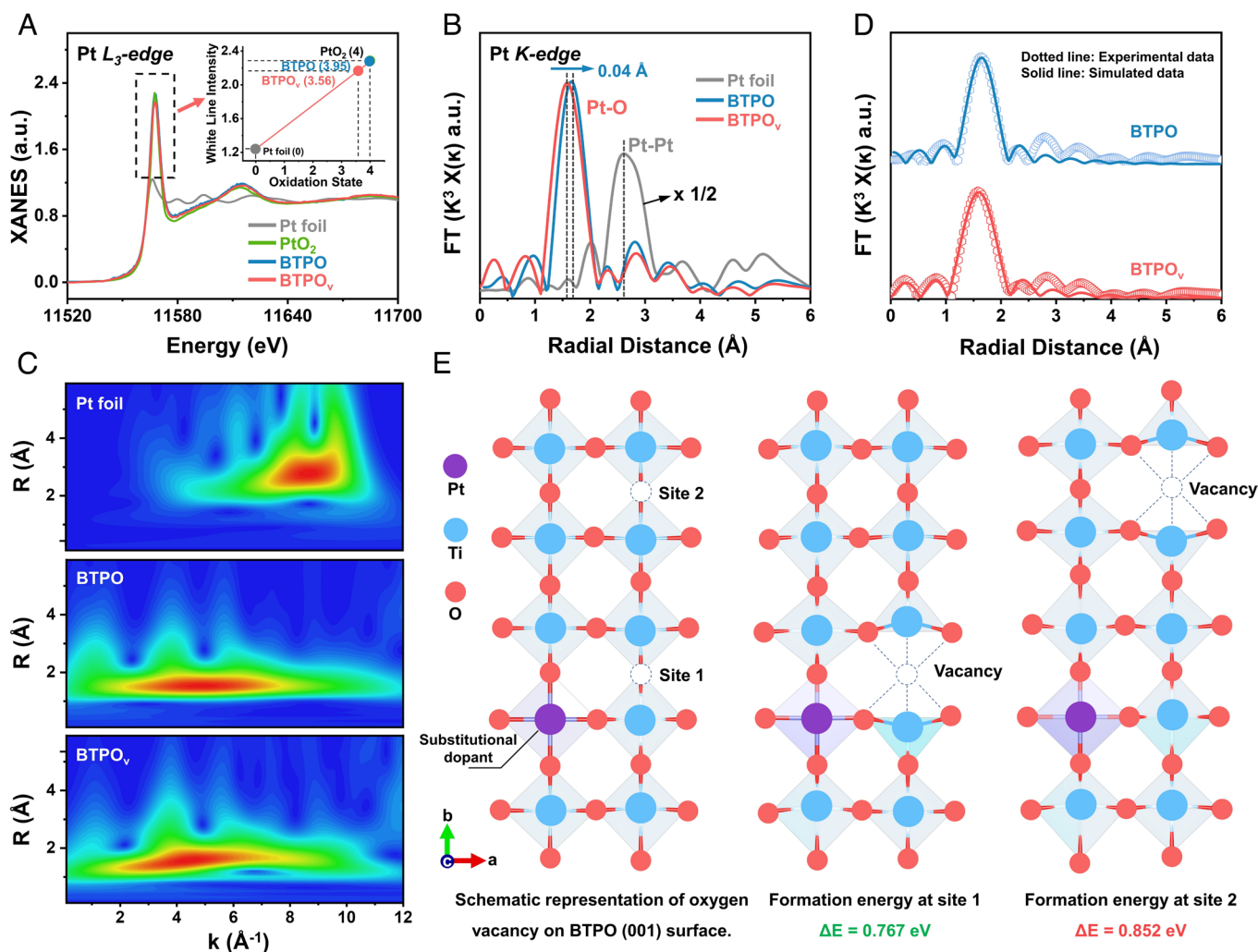


**Fig. 2.** Chemical structure and coordination information. (A) Normalized Pt  $L_3$ -edge XANES spectra of BTPO, BTPO<sub>v</sub>, standard Pt foil, and PtO<sub>2</sub>. The inset shows the average valence state of Pt in BTPO and BTPO<sub>v</sub>. (B) FT-EXAFS spectra of BTPO, BTPO<sub>v</sub>, and standard Pt foil. (C) WT plots of Pt foil, BTPO and BTPO<sub>v</sub>. (D) FT-EXAFS fitting curves of BTPO and BTPO<sub>v</sub> at R space. (E) Calculated oxygen vacancy formation energies on BTPO (001) surface.

The PHE rates of BTO and BTO<sub>v</sub> are 35 and 41  $\mu\text{mol}\cdot\text{g}^{-1}\cdot\text{h}^{-1}$ , while in BTPO the PHE rate can be increased to 254  $\mu\text{mol}\cdot\text{g}^{-1}\cdot\text{h}^{-1}$ , which may be due to the effective proton reduction at the Pt sites (35). The BTPO<sub>v</sub> catalyst with unique Pt-O-Ti<sup>3+</sup> site exhibited the optimal PHE rate of 1519  $\mu\text{mol}\cdot\text{g}^{-1}\cdot\text{h}^{-1}$ , nearly 43, 37, and 6 times for BTO, BTO<sub>v</sub>, and BTPO, respectively (Fig. 3B). Moreover, the corresponding time-resolved MOX degradation was displayed in Fig. 3C and *SI Appendix*, Fig. S19. The MOX degradation of different catalysts including BTO, BTO<sub>v</sub>, and BTPO were studied for comparison. The MOX removal of BTO, BTO<sub>v</sub>, and BTPO reach 5%, 6% and 45% within 90 min, respectively. In contrast, the MOX adsorption on BTPO<sub>v</sub> is enhanced four times and almost 100% of MOX is removed within 90 min. The degradation kinetic model ( $k$  value) of MOX degradation on BTO, BTO<sub>v</sub>, and BTPO are calculated to be 0.00049  $\text{min}^{-1}$ , 0.00058  $\text{min}^{-1}$ , and 0.00667  $\text{min}^{-1}$ . By contrast, the  $k$  value of BTPO<sub>v</sub> is 0.048  $\text{min}^{-1}$ , nearly 98, 83, and 7.2 times higher than that of BTO, BTO<sub>v</sub>, and BTPO, respectively. Impressively, the BTPO<sub>v</sub> shows an exceptional atomic economy with the best H<sub>2</sub> production TOF (370 h<sup>-1</sup>) among the recently reported dual-functional photocatalysts (*SI Appendix*, Fig. S20). In addition, the BTPO<sub>v</sub> catalyst outperformed most of the recently reported dual-functional photocatalysts of pollutant removal performance, showing strong environmental remediation capabilities (Fig. 3D

and *SI Appendix*, Table S4). To further confirm the active species of MOX degradation, trapping experiments were conducted. As shown in Fig. 3E, the addition of 0.01 M tert-butanol (scavenger for •OH) and 0.005 M EDTA-2Na (scavenger for hole) can reduce the degradation rate to 91% and 51%, respectively. MOX oxidation activity is drastically restrained by EDTA-2Na, indicating that hole is the primary degradation active specie (36). Meanwhile, after four cycles of testing, the BTPO<sub>v</sub> system still maintains an initial hydrogen production and degradation performance above 80% (Fig. 3F) and shows high structural stability (*SI Appendix*, Fig. S21). Importantly, BTPO<sub>v</sub> has broad adaptability to a wide range of wastewaters and also exhibits excellent PHE performance in other persistent organic contaminants such as levofloxacin, ciprofloxacin, ofloxacin, norfloxacin, gatifloxacin, tetracycline, rhodamine B, and pefloxacin (*SI Appendix*, Fig. S22), showing great potential for practical environmental remediation hydrogen production applications.

**Charge Separation and Transfer Mechanism on Pt-O-Ti<sup>3+</sup> Site.** To explain the origin of this interesting dual-functional photocatalytic activity, the influence of the Pt-O-Ti<sup>3+</sup> site on the separation and transfer of photoinduced charge was carefully studied. Ultraviolet-visible (UV-vis) diffuse reflectance spectra and valence band X-ray photoelectron spectroscopy (*SI Appendix*, Figs. S23–S25) were used

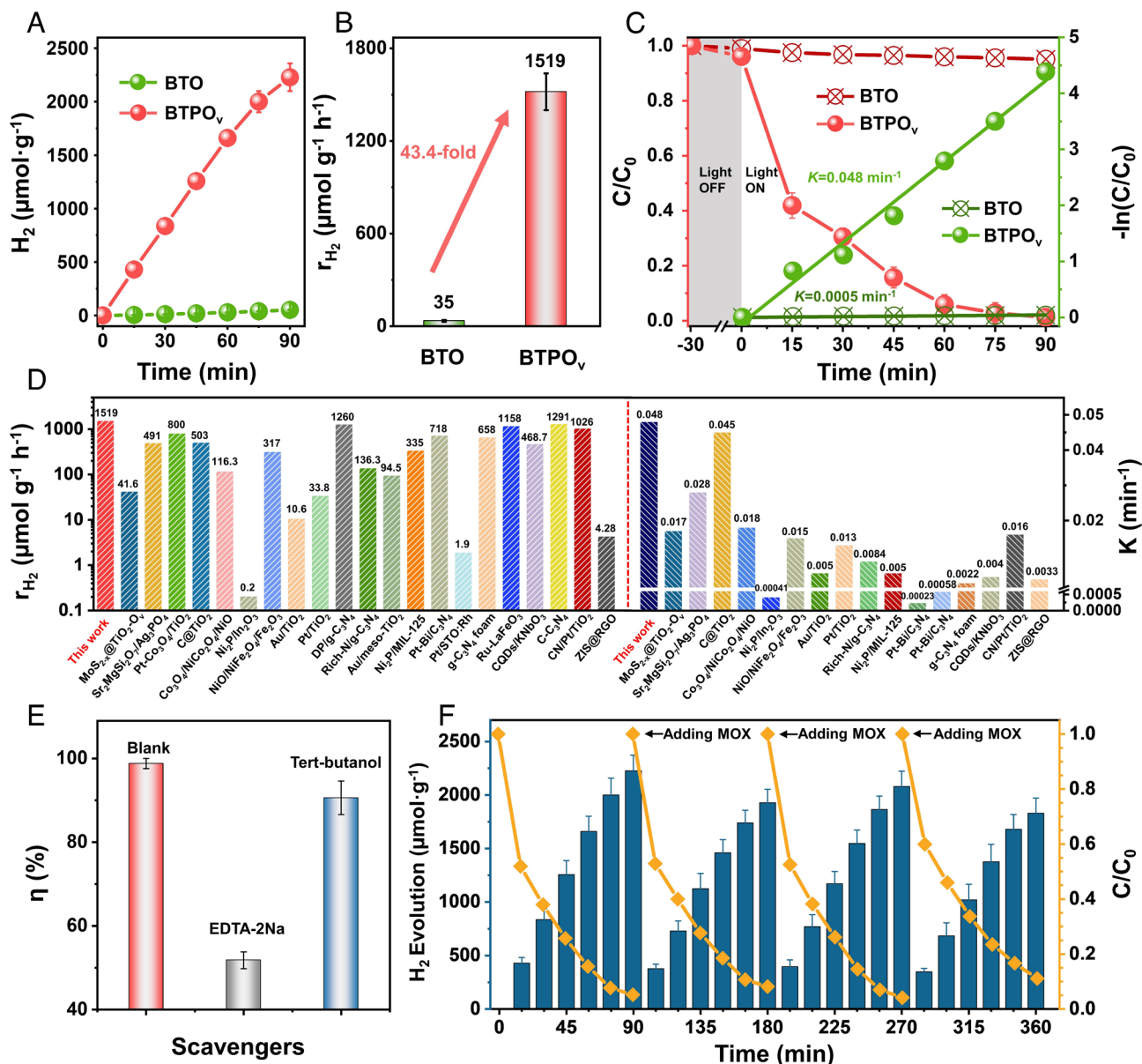


**Fig. 3.** Dual-functional photocatalytic performance. (A) Time courses of PHE on BTO and BTPO<sub>v</sub>. (B) PHE rates of BTO and BTPO<sub>v</sub>. (C) Degradation and first-order reaction kinetics of MOX removal in BTO and BTPO<sub>v</sub> photocatalytic system under PHE process. (D) Performance comparison of recently reported dual-functional photocatalysts. (E) MOX degradation performance in the presence of radical scavengers. (F) Dual-photocatalytic activity and stability of BTPO<sub>v</sub> catalyst. Reaction conditions: [MOX] = 20 mg·L<sup>-1</sup>; [Catalyst] = 0.2 g·L<sup>-1</sup>; [Temp] = 288 K. Error bars represent SDs from triplicate experiments (n = 3).

to measure the band structure, where BTO, BTPO, and BTPO<sub>v</sub> have similar alignments, so that the main contribution of the band structure can be excluded (37). Photoinduced charge transfer from the photocatalyst to the surface is a key step in photocatalysis. The steady-state surface photovoltage (SS-SPV) can directly evaluate the intensity of the internal electric field caused by the charge transfer process. Compared to BTO and BTPO, BTPO<sub>v</sub> has no significant surface photovoltage response in the 300 to 400 nm range, which is due to the rapid trapping of photoinduced charges by Ti<sup>3+</sup> defects (Fig. 4A) (38). The recombination rate of photoinduced charges trapped to the surface (microsecond) is much higher than that of the time required for photocatalytic surface reactions (milliseconds), rapid separation of trapped charges on the surface is essential to improve photocatalytic reaction activity (20). The X-ray photoelectron spectroscopy (XPS) was first used to analyze the electron transfer (SI Appendix, Fig. S26). The high-resolution Ti 2p spectra show a blue shift (0.15 eV) in BTO<sub>v</sub>, which are

likely to be related to the occurrence of oxygen vacancies and the decreasing average valence state of Ti, while BTPO<sub>v</sub> shows a relatively smaller blue shift (0.05 eV), which is probably due to the local charge redistribution caused by the doping of Pt atoms. To explore the origin of the interesting difference, Ti *K-edge* XANES was used to further analyze the difference between Ti species in BTO<sub>v</sub> and BTPO<sub>v</sub> (Fig. 4B). The absorption edge ( $E_0$ ) of BTPO<sub>v</sub> shifts to the direction of high energy, demonstrating that the valence state of Ti species in BTPO<sub>v</sub> is higher than that of BTO<sub>v</sub>. Further linear combination analysis of XANES spectra (SI Appendix, Fig. S27) confirms that the content of Ti<sup>3+</sup> species in BTO<sub>v</sub> is higher than BTPO<sub>v</sub> (28% in BTPO<sub>v</sub> and 44% in BTO<sub>v</sub>) (39). In contrast, the Pt 4f XPS spectrum of BTPO<sub>v</sub> is shifted to lower binding energy compared to BTPO, which implies that electron accumulation on Pt atoms, in agreement with the results obtained from Pt *L<sub>3</sub>-edge* XANES (Fig. 2A and SI Appendix, Fig. S28). Thus, the doping of Pt atom causes a surface electronic

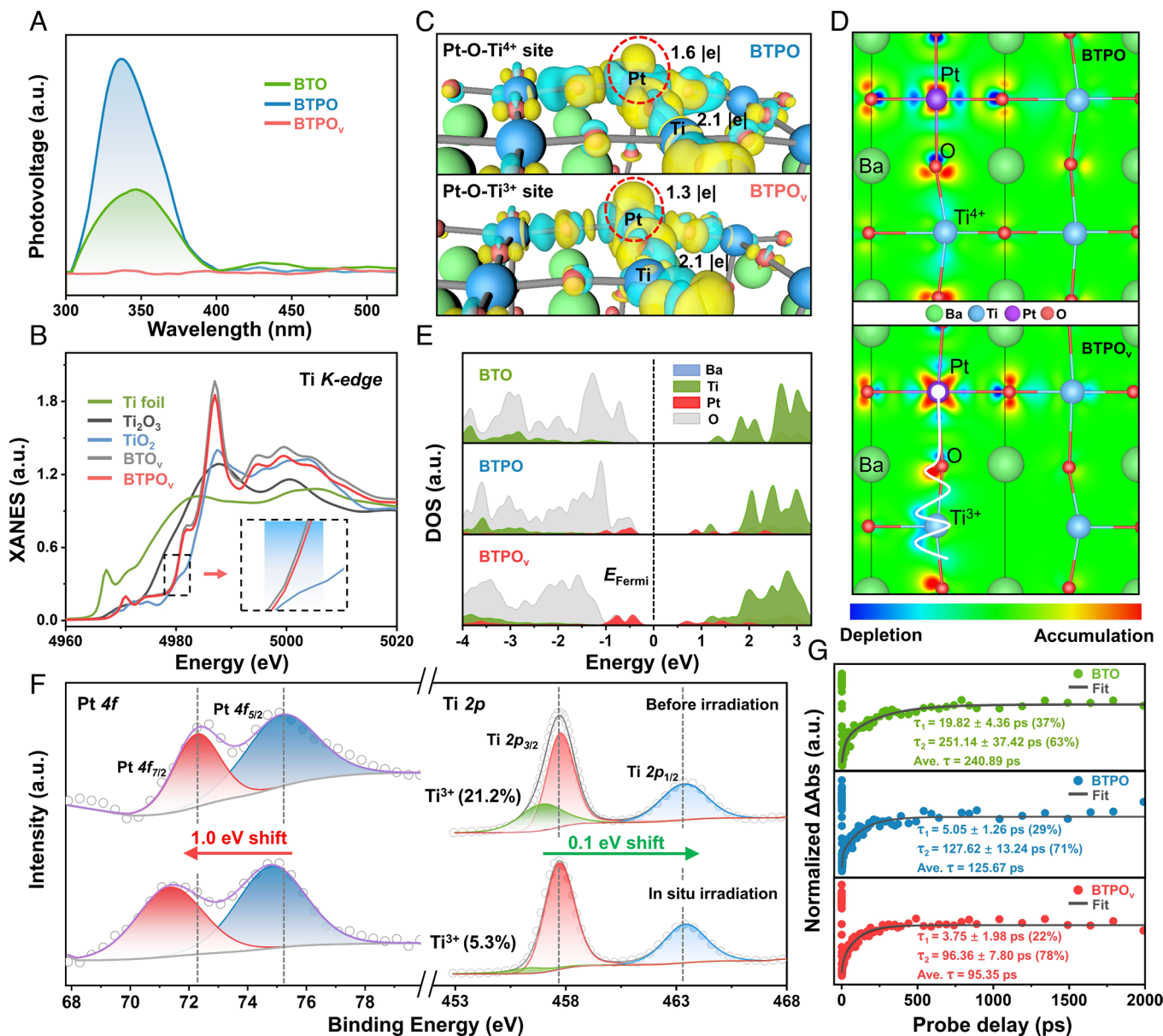


**Fig. 4.** Charge separation and transfer mechanism (A) SS-SPV responses of BTO, BTPO and BTPO<sub>v</sub>. (B) Normalized Ti *K*-edge XANES spectra of BTPO<sub>v</sub>, BTPO, standard Ti foil, Ti<sub>2</sub>O<sub>3</sub> and TiO<sub>2</sub>. (C) Calculated charge density difference and Bader charge in BTPO and BTPO<sub>v</sub>. The cyan and yellow areas represent electron depletion and accumulation, respectively. (D) Top view of the charge distribution in BTPO and BTPO<sub>v</sub>. (E) DOS profiles of BTPO, BTPO and BTPO<sub>v</sub>. (F) In situ irradiation XPS spectra of Pt 4*f* and Ti 2*p* of BTPO<sub>v</sub>. (G) TAS kinetics probed at 620 nm for BTO, BTPO and BTPO<sub>v</sub>.

redistribution and reduces the electron density of Ti atoms (34). To better understand the effect of the Pt-O-Ti<sup>3+</sup> site on the local charge at the atomic-level, DFT calculations were performed to investigate the electron transfer mechanism. Fig. 4C shows the charge density difference of the Pt-O-Ti<sup>3+</sup> site. Around the Pt atom, there is a larger electron accumulation area in BTPO<sub>v</sub>, than in BTPO, while a larger electron depletion area exists around the Ti atom, which is consistent with the XANES and XPS results. Top view of the charge distribution shown in Fig. 4D and SI Appendix, Fig. S29, there is no obvious electron transfer in the Pt-O-Ti<sup>4+</sup> site of BTPO. Instead, the cyan region covers the entire Pt-O-Ti<sup>3+</sup> site in BTPO<sub>v</sub> forming an electron transfer bridge and an electron accumulation area on the Pt atom. The Bader charge analysis further quantifies the differences in charge densities, the charge of Ti, O and Pt atoms in BTPO is calculated to be +2.1 |e|, -1.1 |e| and +1.6 |e|, compared to +2.1 |e|, -1.1 |e|, and +1.3 |e| in BTPO<sub>v</sub>, respectively, demonstrating that Ti<sup>3+</sup> defects caused by oxygen vacancies can conduct 3d<sup>1</sup> electrons to Pt atoms through

oxygen ligand bridges (SI Appendix, Table S5). The resulting charge redistribution between Ti and Pt atoms (Ti<sup>3+</sup> + Pt<sup>4+</sup> → Ti<sup>4+</sup> + Pt<sup>3+</sup>) is deduced to produce superexchange interaction between the adjacent Ti (IV) and Pt (III) sites (SI Appendix, Fig. S30) (40). Since the Pt-Ti superexchange is mediated by the lattice oxygen in the perovskite oxides, the interaction should be significantly affected by the orbital coupling between Pt/Ti 3d and O 2p. Analysis of the surface partial density of states (PDOS) in BTPO<sub>v</sub> (Fig. 4E), shows a pronounced orbital hybridization occurs between the introduced Pt and the Ti/O atom after the loading of the Pt atoms, which promotes the transfer of electrons from the Ti/O atom to the Pt site and facilitates the following proton reduction process (12, 41). To investigate the real electron transfer of the photocatalyst during the photocatalytic reaction, in situ irradiation XPS of BTPO<sub>v</sub> before and during the irradiation was monitored. The Pt 4*f* spectra consist of two Gaussian peaks corresponding to Pt<sup>4+</sup> at 75.3 and 72.4 eV, with a blue shift to 74.7 and 71.2 eV after irradiation, indicating a partial reduction of Pt<sup>4+</sup>. In contrast, the Ti atom is

oxidized during the irradiation ( $\text{Ti}^{3+}/\text{Ti}^{4+}$  ratio of 0.27 vs. 0.06) (Fig. 4F). These results confirm that the Pt-O-Ti<sup>3+</sup> site effectively separates photogenerated carriers and Ti<sup>3+</sup> defects can be used as a hole trapping site.

To further verify the enhanced carrier dynamics due to the site of Pt-O-Ti<sup>3+</sup>, photoluminescence (PL) spectra, electrochemical impedance spectroscopy (EIS) and transient photocurrent curves (TPC) measurements were performed. Due to the similar light absorption and band structures of the samples, the results obtained can be used to discuss the efficiency of charge separation/transfer. The PL spectrum of BTPO<sub>v</sub> exhibits the lowest radiative recombination quenching signal of photogenerated electrons and holes, which indicates that the Pt-O-Ti<sup>3+</sup> site can effectively improve the charge separation efficiency (SI Appendix, Fig. S31). As shown in EIS spectra (SI Appendix, Fig. S32), the smallest arc radius indicates the smallest charge transfer resistance of BTPO<sub>v</sub> under photocatalytic conditions. In addition, the TPC results show that the photocurrent of BTPO<sub>v</sub> is much higher than that of both BTO and BTPO (SI Appendix, Fig. S33) (33, 37). This demonstrates that the Pt-O-Ti<sup>3+</sup> site can significantly improve the separation efficiency of photoinduced charges and reduce the transfer resistance, thus improving the photocatalytic activity. After that, the charge transport dynamics of BTPO<sub>v</sub> was further investigated using femtosecond transient absorption (TA) spectroscopy (Fig. 4G and SI Appendix, Fig. S34). The pump pulse with wavelength 365 nm can effectively promote electrons from valence band to conduction band. The results show that similar charge transport dynamics are observed in all samples, with excited state absorption occurring between 500 and 650 nm, which can reflect the lifetime of photoexcited electrons. The negative absorption signal observed in the 650 to 700 nm range is attributed to the processes of ground-state bleaching and stimulated radiation. Representative data was obtained at 620 nm, because the positive absorption region at 500 to 650 nm can better describe the electron relaxation process (42, 43). The results show that the kinetic decay curves of all prepared samples have an instantaneous accumulation of TA intensity and then decay in a bi-exponential manner. The decay component  $\tau_1$  reveals the trapping of electrons from conduction band into trapped state, and the component  $\tau_2$  indicates the recombination of trapped electrons and holes (44). The bi-exponential fitting results are  $\tau_1 = 19.82 \pm 4.36$  ps (37%) and  $\tau_2 = 251.14 \pm 37.42$  ps (63%) for BTO,  $\tau_1 = 5.05 \pm 1.26$  ps (29%) and  $\tau_2 = 127.62 \pm 13.24$  ps (71%) for BTPO,  $\tau_1 = 3.75 \pm 1.98$  ps (22%) and  $\tau_2 = 96.36 \pm 7.80$  ps (78%) for BTPO<sub>v</sub>. The fitted average lifetimes for BTO, BTPO and BTPO<sub>v</sub> are 240.89, 125.67 and 95.35 ps, respectively. The almost 2.5-fold decrease in the average lifetime over BTPO<sub>v</sub> compared with pristine BTO could be ascribed to the efficient electron transfer caused by the superexchange effect (23, 40). In addition, the accelerated time constant  $\tau_1$  (3.75 ps) of BTPO<sub>v</sub> also proves the ultrafast charge capture on the Ti<sup>3+</sup> defects. The time-resolved photoluminescence spectra conclusion is consistent with the TA analysis (SI Appendix, Fig. S35 and Table S6), indicating that the Pt-O-Ti<sup>3+</sup> site boosts charge trapping and transfer processes. Combining experimental and DFT calculations, the oxygen vacancies play the role of aggregating photogenerated charge and the adjacent Ti<sup>3+</sup> defects allow rapid transfer of electrons to Pt atoms through the 180° superexchange effect. At the same time, the holes would be restricted to Ti<sup>3+</sup> defects, which promotes the subsequent oxidation process of the organic contaminant.

**Surface Reaction Mechanism.** To better understand the underlying dual-functional reaction mechanism on BTPO<sub>v</sub>, DFT calculations for thermodynamic aspects were performed. The reaction barriers for PHE on BTO, BTPO, and BTPO<sub>v</sub> surfaces were first calculated

(Fig. 5A), calculated free energy for H<sup>+</sup> adsorption ( $\Delta G_{\text{H}}$ ) value of BTPO<sub>v</sub> is only -0.36 eV, which is closer to 0 eV (the ideal free energy) than BTO (1.31 eV) and BTPO (-0.56 eV) (42). In addition, Pt-O-Ti<sup>3+</sup> sites can provide almost double the electrons when adsorbing H<sup>+</sup>, thus promoting proton reduction and improving its reactivity (Fig. 5B and SI Appendix, Fig. S36). By regulating the binding strength of contaminants on the catalyst surface, the catalytic activity can be significantly increased and eliminating the electron depletion caused by free organic contaminants (23, 45). The interactions between MOX molecules and Pt-O-Ti<sup>3+</sup> sites were further investigated by constructing optimized adsorption conformations of MOX on BTO, BTPO and BTPO<sub>v</sub> surfaces. The MOX molecule exhibits the lowest electrostatic potential (-0.12 |e|) at the terminal oxygen site and the Ti atoms with the highest charge (+2.0 |e|) are identified as the best adsorption sites (Fig. 5C and SI Appendix, Table S5). The adsorption energy of MOX on the Ti<sup>3+</sup> sites in BTPO<sub>v</sub> surface ( $\Delta E_{\text{ads}} = -2.11$  eV) is raised drastically than that of Ti<sup>4+</sup> sites (-1.71 eV in BTO and -1.29 eV in BTPO), which indicates that unsaturated coordination of Ti atoms due to oxygen vacancies can enhance the chemical adsorption reaction activity of the MOX (Fig. 5D) (46). The ultra-performance liquid chromatography-mass spectrometry (UPLC-MS) was used to identify the intermediate products during the degradation of MOX. Fig. 5E shows the chromatograms of the MOX solutions at different degradation intervals. The results showed the notable peak of  $m/z = 402$  at a retention time of 2.5 min is related to MOX, which decayed with time and nearly disappeared after 90 min of reaction, this result is consistent with the almost 100% removal of MOX at 90 min (Fig. 3C). The ecotoxicity of the most significant degradation products with a retention time of 3 min ( $m/z = 293$ ) and 2.6 min ( $m/z = 321$ ) is significantly reduced and the leakage of Pt atoms is located at safe values throughout the reaction (SI Appendix, Figs. S37 and S38). Based on the analysis of the UPLC-MS chromatogram results, a possible degradation pathway is proposed (SI Appendix, Fig. S39 and Table S7) (47). In summary, as shown in SI Appendix, Fig. S40, the dual-functional photocatalytic mechanism of BTPO<sub>v</sub> in MOX solution via Pt-O-Ti<sup>3+</sup> superexchange effect has been disclosed. The targeted separation of photogenerated carriers is facilitated by of Pt-O-Ti<sup>3+</sup> superexchange effect, including adsorb MOX at Ti sites and optimal H<sup>+</sup> adsorption at Pt sites, collectively contribute to the dual-functional photocatalysis activity of BTPO<sub>v</sub>.

## Conclusions

In summary, we constructed a rapid charge migration path on Pt-doped BaTiO<sub>3</sub> with oxygen vacancies single catalyst, effectively separated photogenerated charges and achieved simultaneous catalytic oxidative and reductive reactions in single catalyst. X-ray absorption spectroscopy and HAADF-STEM demonstrate the dispersed presence of Pt on the catalyst and can facilitate the generation of surface oxygen vacancies in adjacent Ti atoms to form Pt-O-Ti<sup>3+</sup> site. DFT calculations suggest that introducing oxygen vacancies accumulation photoinduced charges on the catalyst surface. The X-ray absorption spectroscopy, XPS spectra and Bader charge reveal that adjacent Ti<sup>3+</sup> (3d<sup>1</sup> configuration) allows rapid migration of electrons to Pt atoms through the 180° superexchange effect, while SS-SPV spectra and in situ XPS confirm the holes will be confined in Ti<sup>3+</sup> defects thus achieving the spatial separation of electrons and holes under photocatalytic process. Moreover, the femtosecond transient absorption spectroscopy confirms significantly enhanced charge transportation dynamics. Finally, Pt sites exhibit optimal free energy for H<sup>+</sup> adsorption and H<sub>2</sub> desorption, as well as Ti<sup>3+</sup> sites with the strongest MOX chemical adsorption

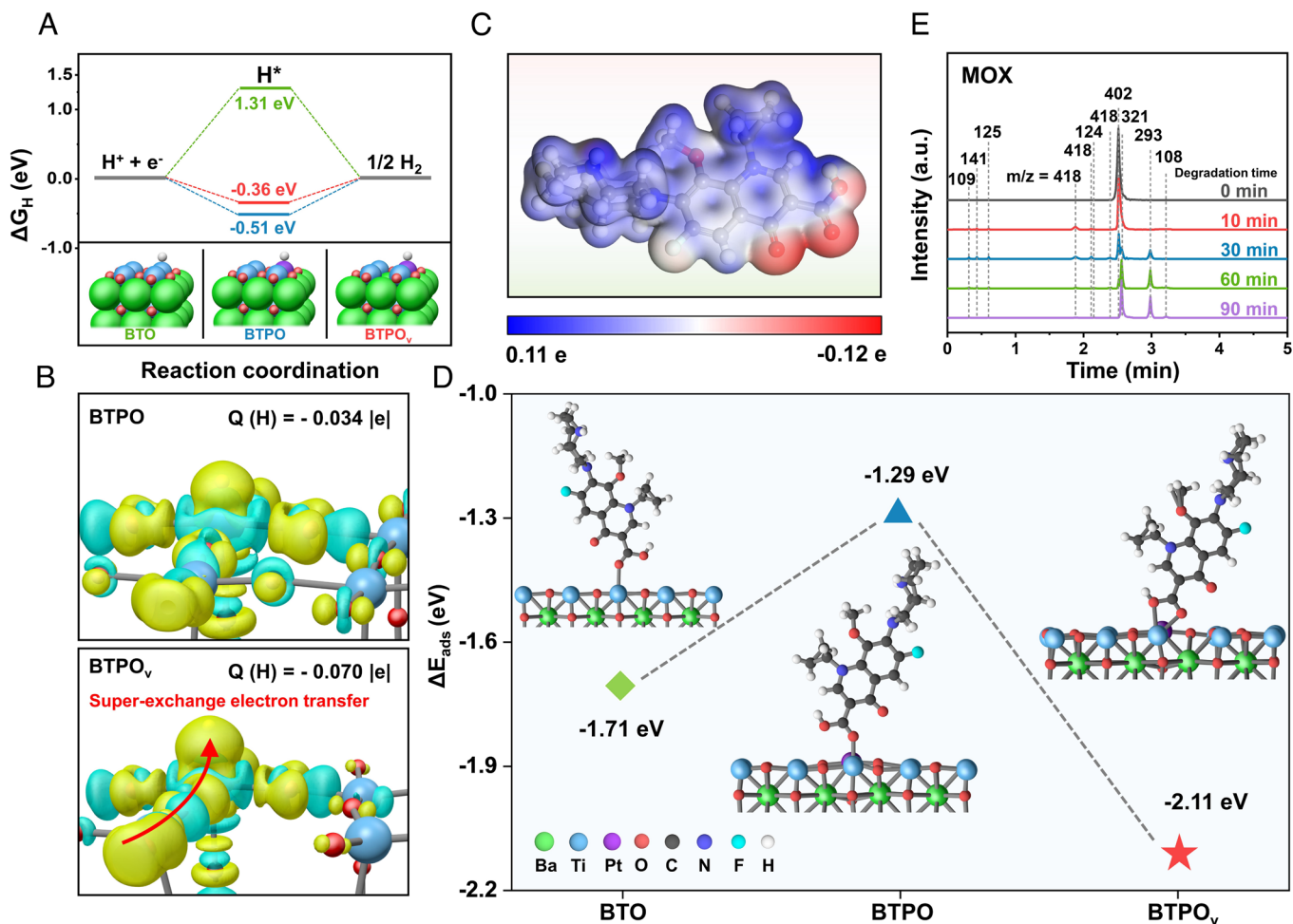


**Fig. 5.** Surface reaction mechanism. (A) Free-energy diagrams for the PHE on BTO, BTPO, and BTPO<sub>v</sub>. (B) Calculated charge density difference and Bader charge under H<sup>+</sup> adsorption. (C) The calculated electrostatic potential of MOX molecule. (D) Adsorption energy of MOX on BTO, BTPO, and BTPO<sub>v</sub> surface. (E) UPLC-MS chromatograms of the reaction solution at different degradation time intervals.

reaction activity. As an outcome, the BTPO<sub>v</sub> showed excellent HER activity ( $1,519 \mu\text{mol}\cdot\text{g}^{-1}\cdot\text{h}^{-1}$ ) in MOX solution with a TOF value of  $370.4\cdot\text{h}^{-1}$ , obviously higher than the recent reported dual-functional photocatalysts, while achieving 98.8% MOX removal efficiency within 90 min. This work explores strategies to develop advanced materials for dual-functional photocatalysis by building multi-active-site over single catalyst through physically relevant effects for coupling various challenging reactions.

## Materials and Methods

**Preparation of Catalyst.** Typically,  $\text{C}_{16}\text{H}_{36}\text{O}_4\text{Ti}$  (5.0 mmol) was slowly added into 10 mL of ethanolamine solution and agitated, to which NaOH (4.8 M, 25.0 mL) and  $\text{BaCl}_2\cdot 2\text{H}_2\text{O}$  (1.0 M, 5.0 mL) were added and stirred for 0.5 h. The obtained suspension solution was then sealed into a Teflon autoclave (100 mL) and kept at 180 °C for 24 h. The obtained product (BTO) was washed with deionized water and ethanol several times and dried at 60 °C in vacuum oven. Next, 0.2 g BTO was dispersed into 60 ml deionized water for 10 min ultrasonic. 0.135 ml  $\text{H}_2\text{PtCl}_6$  solution ( $1.48 \text{ mg}_P\cdot\text{mL}^{-1}$ ) was slowly dropped into the suspension under vigorous stirring. The solution was stirred at 70 °C for 6 h and then natural cooled to obtain BTPO. The obtained BTPO was heated in Ar atmosphere at 400 °C for 10 h to form surface oxygen vacancy to obtain BTPO<sub>v</sub>. The obtained BTO was heated in Ar atmosphere at 400 °C for 10 h to form surface oxygen vacancy to obtain BTO<sub>v</sub>.

**Experimental Procedures and Analyses.** Photocatalytic reactions were carried out in a gas-closed system. Typically, 20 mg photocatalyst was dispersed by stirrer in 100 mL MOX solution ( $20 \text{ mg L}^{-1}$ ) with stirring for 30 min under dark conditions to establish adsorption-desorption equilibrium before light irradiation.

The light source is a 300 W Xe lamp with AM 1.5G filter (light intensity of  $370 \text{ W m}^{-2}$ ). The amount of hydrogen was analyzed using a gas chromatography. The aqueous solutions were sampled at 15-min intervals, filtered using a  $0.22\text{-}\mu\text{m}$  polyether sulfone filter and further measured for contaminant concentrations by chromatograph. After each sampled, the system was pumped for 30 min to regain the vacuum state. During the photocatalytic reaction, the temperature of the solution was kept below 288 K by a cooling water bath.

The general catalytic reaction occurs on the surface of the catalyst, and the TOF is calculated based on the available active surface atoms.

$$\text{TOF} [\text{h}^{-1}] = \frac{\text{the number of moles of hydrogen evolution}}{\text{the total number of active atoms} \times \text{time}} = \frac{n(\text{H}_2)}{n(\text{Pt}) \times t}$$

The reaction kinetics for the degradation of the above contaminants is analyzed using the following.

$$\ln\left(\frac{C_t}{C_0}\right) = k \times t$$

where  $C_t$  and  $C_0$  are the concentration of pollutants at reaction time ( $t$ ) and initial time ( $0$ ), respectively, and  $k$  is the first-order kinetic constant ( $\text{min}^{-1}$ ).

**Femtosecond Transient Absorption Spectroscopy.** The Femtosecond transient absorption spectroscopy were measured in the combined utilization of the Femtosecond Laser System (Coherent) and the Helios Pump-Probe System (Ultrafast Systems LLC), which was a commonly utilized time-resolving method and was considered to be one of the most effective tools for detecting the dynamics information in electronic excited state. The 365-nm pump pulses were generated from optical parametric amplifier (TOPAS-800-fs), which was pumped by the

800 nm fundamental beam output from Femtosecond Laser System. The white light continuum probe beam was generated by focusing a small portion (~10 μJ) of the regenerative amplifier's fundamental 800 nm laser pulses into a 2-mm sapphire crystal. The pump and probe beams intersect on the sample at a particular angle. In order to achieve high signal-to-noise ratios, five to ten scans of the data were collected in the measurement and the signal amplitude in the femtosecond transient absorption measurements were averaged for further analysis.

**X-ray Absorption Spectroscopy Measurements.** The X-ray absorption fine structure spectra (Pt L<sub>3</sub>-edge and Ti K-edge) were obtained at 1W1B station in Beijing Synchrotron Radiation Facility (BSRF). The storage rings of BSRF were operated at 2.5 GeV with a maximum current of 250 mA. Using Si (111) double-crystal monochromator, the data collection was carried out in transmission mode using ionization chamber. All spectra were collected at ambient conditions.

**Calculation Details.** First-principle calculations were performed by the DFT with the Vienna ab initio simulation package (48). The generalized gradient approximation with the Perdew–Burke–Ernzerhof functional was used to describe the electronic exchange and correlation effects (49–51). Structure relaxation proceeded until all forces on atoms were less than 1 meV Å<sup>-1</sup> and the total stress tensor was within 0.01 GPa of the target value. The BO<sub>2</sub>-terminated (001) plane

was chosen to model the reaction surface of BTPO, because in cubic-symmetry perovskites this is the most obvious and stable termination.

**Data, Materials, and Software Availability.** All study data are included in the article and *SI Appendix*.

**ACKNOWLEDGMENTS.** We gratefully acknowledge the financial support by the Natural Science Foundation of China as general projects (grant Nos. 2225604, 22076082, 21874099, 22176140, 22006029, and 42277059), the Tianjin Commission of Science and Technology as key critical technologies R&D projects (grant No. 21YFNSN00250), the Frontiers Science Center for New Organic Matter (grant No. 63181206), and Haihe Laboratory of Sustainable Chemical Transformations.

Author affiliations: <sup>a</sup>MOE Key Laboratory of Pollution Processes and Environmental Criteria/Tianjin Key Laboratory of Environmental Remediation and Pollution Control, College of Environmental Science and Engineering, Nankai University, 300350 Tianjin, China; <sup>b</sup>School of Environmental Science and Engineering, Tiangong University, 300387 Tianjin, China; <sup>c</sup>School of Energy and Environmental Engineering, Hebei University of Technology, 300401 Tianjin, China; and <sup>d</sup>Tianjin Key Laboratory of Molecular Optoelectronic Sciences Department of Chemistry, School of Science, Collaborative Innovation Center of Chemical Science and Engineering, Tianjin University, 300072 Tianjin, China

- J. L. Wilkinson *et al.*, Pharmaceutical pollution of the world's rivers. *Proc. Natl. Acad. Sci. U.S.A.* **119**, e2113947119 (2022).
- B. Van der Bruggen, Sustainable implementation of innovative technologies for water purification. *Nat. Rev. Chem.* **5**, 217–218 (2021).
- Y. Gao *et al.*, Unraveling the high-activity origin of single-atom iron catalysts for organic pollutant oxidation via peroxymonosulfate activation. *Environ. Sci. Technol.* **55**, 8318–8328 (2021).
- F. Sun *et al.*, Energy-saving hydrogen production by chlorine-free hybrid seawater splitting coupling hydrazine degradation. *Nat. Commun.* **12**, 4182 (2021).
- W. Shang *et al.*, Synergistic redox reaction for value-added organic transformation via dual-functional photocatalytic systems. *ACS Catal.* **11**, 4613–4632 (2021).
- M. Du *et al.*, Trash to treasure: Photoreforming of plastic waste into commodity chemicals and hydrogen over MoS<sub>2</sub>-tipped CdS nanorods. *ACS Catal.* **12**, 12823–12832 (2022).
- W. Liu *et al.*, Directing charge transfer in a chemical-bonded BaTiO<sub>3</sub>@ReS<sub>2</sub> Schottky heterojunction for piezoelectric enhanced photocatalysis. *Adv. Mater.* **34**, 2202508 (2022).
- L. Zhang *et al.*, Molecular oxidation-reduction junctions for artificial photosynthetic overall reaction. *Proc. Natl. Acad. Sci. U.S.A.* **119**, e2210550119 (2022).
- A. Prominski *et al.*, Porosity-based heterojunctions enable leadless optoelectronic modulation of tissues. *Nat. Mater.* **21**, 647–655 (2022).
- Y. Zhao *et al.*, Simultaneous oxidative and reductive reactions in one system by atomic design. *Nat. Catal.* **4**, 134–143 (2021).
- R. Chen *et al.*, Spatiotemporal imaging of charge transfer in photocatalyst particles. *Nature* **610**, 296–301 (2022).
- G. Wang *et al.*, Synergistic modulation of the separation of photo-generated carriers via engineering of dual atomic sites for promoting photocatalytic performance. *Adv. Mater.* **33**, 2105904 (2021).
- G. Wang, Z. Chen, T. Wang, D. Wang, J. P. Mao, Cu dual sites on graphitic carbon nitride for photocatalytic CO<sub>2</sub> reduction to hydrocarbon fuels with high C<sub>2</sub>H<sub>6</sub> evolution. *Angew. Chem. Int. Ed. Engl.* **61**, e202210789 (2022).
- P. Zhou *et al.*, Solar-to-hydrogen efficiency of more than 9% in photocatalytic water splitting. *Nature* **613**, 66–70 (2023).
- B. Moss *et al.*, Linking in situ charge accumulation to electronic structure in doped SrTiO<sub>3</sub> reveals design principles for hydrogen-evolving photocatalysts. *Nat. Mater.* **20**, 511–517 (2021).
- Z. Yang *et al.*, Ultrafast self-trapping of photoexcited carriers sets the upper limit on antimony trisulfide photovoltaic devices. *Nat. Commun.* **10**, 4540 (2019).
- J. B. Muir *et al.*, Interactions between Fermi polarons in monolayer WS<sub>2</sub>. *Nat. Commun.* **13**, 6164 (2022).
- J. Cai *et al.*, Synergistic enhancement of light harvesting and charge separation over surface-disorder-engineered TiO<sub>2</sub> photonic crystals. *Chem* **2**, 877–892 (2017).
- S. Corby, R. R. Rao, L. Steier, J. R. Durrant, The kinetics of metal oxide photoanodes from charge generation to catalysis. *Nat. Rev. Mater.* **6**, 1136–1155 (2021).
- X. Tao, Y. Zhao, S. Wang, C. Li, R. Li, Recent advances and perspectives for solar-driven water splitting using particulate photocatalysts. *Chem. Soc. Rev.* **51**, 3561–3608 (2022).
- P. Goel *et al.*, Perovskite materials as superior and powerful platforms for energy conversion and storage applications. *Nano Energy* **80**, 105552 (2021).
- W. Zhang, L. K. Ono, J. Xue, Y. Qi, Atomic level insights into metal halide perovskite materials by scanning tunneling microscopy and spectroscopy. *Angew. Chem. Int. Ed. Engl.* **61**, e202112352 (2022).
- Z. Y. Guo *et al.*, Electron delocalization triggers nonradical Fenton-like catalysis over spinel oxides. *Proc. Natl. Acad. Sci. U.S.A.* **119**, e2201607119 (2022).
- X. Liu *et al.*, In situ modulation of A-site vacancies in LaMnO<sub>3,15</sub> perovskite for surface lattice oxygen activation and boosted redox reactions. *Angew. Chem. Int. Ed. Engl.* **60**, 26747–26754 (2021).
- D. Zhong *et al.*, Insights into the synergy effect of anisotropic 001 and {230} facets of BaTiO<sub>3</sub> nanocubes sensitized with CdSe quantum dots for photocatalytic water reduction. *Appl. Catal. B* **227**, 1–12 (2018).
- Z. Zhao *et al.*, Magnetic-field-stimulated efficient photocatalytic N<sub>2</sub> fixation over defective BaTiO<sub>3</sub> perovskites. *Angew. Chem. Int. Ed. Engl.* **60**, 11910–11918 (2021).
- K. Lan *et al.*, Stable Ti<sup>3+</sup> defects in oriented mesoporous titania frameworks for efficient photocatalysis. *Angew. Chem. Int. Ed. Engl.* **59**, 17676–17683 (2020).
- Q. Tang *et al.*, Enhanced piezocatalytic performance of BaTiO<sub>3</sub> nanosheets with highly exposed 001 facets. *Adv. Funct. Mater.* **32**, 2202180 (2022).
- Y. Wang *et al.*, Chemical-pressure-modulated BaTiO<sub>3</sub> thin films with large spontaneous polarization and high Curie temperature. *J. Am. Chem. Soc.* **143**, 6491–6497 (2021).
- D. Zhang *et al.*, Tailoring of electronic and surface structures boosts exciton-triggering photocatalysis for singlet oxygen generation. *Proc. Natl. Acad. Sci. U.S.A.* **118**, e2114729118 (2021).
- Z. Tian *et al.*, Selective photoelectrochemical oxidation of glucose to glucaric acid by single atom Pt decorated defective TiO<sub>2</sub>. *Nat. Commun.* **14**, 142 (2023).
- J. Zhang *et al.*, Novel (Pt-O)<sub>2</sub>(Co-O)<sub>2</sub> nonbonding active structures on defective carbon from oxygen-rich coal tar pitch for efficient HER and ORR. *Adv. Mater.* **34**, e2206960 (2022).
- P. Zhou *et al.*, Single-atom Pt-I<sub>3</sub> sites on all-inorganic Cs<sub>2</sub>SnI<sub>6</sub> perovskite for efficient photocatalytic hydrogen production. *Nat. Commun.* **12**, 4412 (2021).
- Y. Chen *et al.*, Engineering the atomic interface with single platinum atoms for enhanced photocatalytic hydrogen production. *Angew. Chem. Int. Ed. Engl.* **59**, 1295–1301 (2020).
- X. Shi *et al.*, Protruding Pt single-sites on hexagonal ZnIn<sub>2</sub>S<sub>4</sub> to accelerate photocatalytic hydrogen evolution. *Nat. Commun.* **13**, 1287 (2022).
- Y. Gao, Z. Chen, Y. Zhu, T. Li, C. Hu, New insights into the generation of singlet oxygen in the metal-free peroxymonosulfate activation process: Important role of electron-deficient carbon atoms. *Environ. Sci. Technol.* **54**, 1232–1241 (2020).
- X. Ruan *et al.*, A twin S-scheme artificial photosynthetic system with self-assembled heterojunctions yields superior photocatalytic hydrogen evolution rate. *Adv. Mater.* **35**, e2209141 (2022).
- B. Wu *et al.*, Ultrathin porous carbon nitride bundles with an adjustable energy band structure toward simultaneous solar photocatalytic water splitting and selective phenylcarbinol oxidation. *Angew. Chem. Int. Ed. Engl.* **60**, 4815–4822 (2021).
- C. Zhang *et al.*, Ti<sub>1</sub>-graphene single-atom material for improved energy level alignment in perovskite solar cells. *Nat. Energy* **6**, 1154–1163 (2021).
- J. Dai *et al.*, Single-phase perovskite oxide with super-exchange induced atomic-scale synergistic active centers enables ultrafast hydrogen evolution. *Nat. Commun.* **11**, 5657 (2020).
- Y. Wu *et al.*, An organometal halide perovskite supported Pt single-atom photocatalyst for H<sub>2</sub> evolution. *Energy Environ. Sci.* **15**, 1271–1281 (2022).
- X. Zhang *et al.*, Heterostructural CsPbX<sub>3</sub>-PbS (X = Cl, Br, I) quantum dots with tunable Vis-NIR dual emission. *J. Am. Chem. Soc.* **142**, 4464–4471 (2020).
- X. Liu *et al.*, Enhanced localized dipole of Pt-Au single-site catalyst for solar water splitting. *Proc. Natl. Acad. Sci. U.S.A.* **119**, e2119723119 (2022).
- X. Ma, L. Wang, Q. Zhang, H. L. Jiang, Switching on the photocatalysis of metal-organic frameworks by engineering structural defects. *Angew. Chem. Int. Ed. Engl.* **58**, 12175–12179 (2019).
- Q. Zhou *et al.*, Generating dual-active species by triple-atom sites through peroxymonosulfate activation for treating micropollutants in complex water. *Proc. Natl. Acad. Sci. U.S.A.* **120**, e2300085120 (2023).
- Y. Bu *et al.*, Peroxydisulfate activation and singlet oxygen generation by oxygen vacancy for degradation of contaminants. *Environ. Sci. Technol.* **55**, 2110–2120 (2021).
- A. Xu *et al.*, Bio-synthesis of Co-doped FeMnO<sub>4</sub> and its efficient activation of peroxymonosulfate for the degradation of moxifloxacin. *Chem. Eng. J.* **435**, 134695 (2022).
- G. Kresse, J. Furthmüller, Efficient iterative schemes for ab initio total-energy calculations using a plane-wave basis set. *Phys. Rev. B* **54**, 11169–11186 (1996).
- J. P. Perdew, K. Burke, M. Ernzerhof, Generalized gradient approximation made simple. *Phys. Rev. Lett.* **77**, 3865–3868 (1996).
- G. Kresse, D. Joubert, From ultrasoft pseudopotentials to the projector augmented-wave method. *Phys. Rev. B* **59**, 1758–1775 (1999).
- P. E. Blöchl, Projector augmented-wave method. *Phys. Rev. B* **50**, 17953–17979 (1994).